OPEN

Correspondence and
requests for materials
should be addressed to
T.K. (kawano@ee.tut.
ac.jp)

In vivo neuronal action potential recordings via three-dimensional microscale needle-electrode arrays

Akifumi Fujishiro[1], Hidekazu Kaneko[2], Takahiro Kawashima[3], Makoto Ishida[1,4] & Takeshi Kawano[1]

[1]Department of Electrical and Electronic Information Engineering, Toyohashi University of Technology, 1-1 Hibarigaoka Tempaku-cho, Toyohashi, Aichi 441-8580, Japan, [2]National Institute of Advanced Industrial Science and Technology (AIST), AIST Tsukuba Central 6, Higashi, Tsukuba, Ibaraki 305-8566, Japan, [3]Department of Mechanical Engineering, Toyohashi University of Technology, 1-1 Hibarigaoka Tempaku-cho, Toyohashi, Aichi 441-8580, Japan, [4]Electronics-Inspired Interdisciplinary Research Institute (EIIRIS), Toyohashi University of Technology, 1-1 Hibarigaoka Tempaku-cho, Toyohashi, Aichi 441-8580, Japan.

Very fine needle-electrode arrays potentially offer both low invasiveness and high spatial resolution of electrophysiological neuronal recordings *in vivo*. Herein we report the penetrating and recording capabilities of silicon-growth-based three-dimensional microscale-diameter needle-electrodes arrays. The fabricated needles exhibit a circular-cone shape with a 3-μm-diameter tip and a 210-μm length. Due to the microscale diameter, our silicon needles are more flexible than other microfabricated silicon needles with larger diameters. Coating the microscale-needle-tip with platinum black results in an impedance of $\sim$600 kΩ in saline with output/input signal amplitude ratios of more than 90% at 40 Hz–10 kHz. The needles can penetrate into the whisker barrel area of a rat's cerebral cortex, and the action potentials recorded from some neurons exhibit peak-to-peak amplitudes of $\sim$300 μV$_{pp}$. These results demonstrate the feasibility of *in vivo* neuronal action potential recordings with a microscale needle-electrode array fabricated using silicon growth technology.

As microfabrication technologies advance, various types of multichannel microelectrode arrays have been proposed to simultaneously record numerous neurons within a tissue[1–6]. For example, the Michigan electrode is a multi-shank needle array where each needle is approximately 15-μm thick and 50-μm wide[1]. Another major electrode, the Utah electrode, is an array of $\sim$100 needle electrodes where each needle has an $\sim$80-μm diameter at the base[2]. Such devices have been used for chronic recordings from neuronal tissues, including monkey[7] and human cortices[8,9]. Further reducing the needle diameter decreases the invasiveness, allowing for safer device implantation. However, current silicon-etching-based miniaturization technology used to fabricate these electrodes limits the minimum diameter (or width) of the needles to tens of microns with intervals of at least several hundred microns.

To minimize the invasiveness of neuronal activity recordings via needle-electrode arrays, tissue damage due to penetration and movement of the arrays should be reduced. In a tissue, the damaged area, which is occupied by glial cells, is proportional to the needle size (cross-sectional area)[10,11]. Encapsulation of the needle-electrode site with glial cells makes long-term recordings of neuronal activities difficult[11,12]. Thus, the needle diameter should be minimized to reduce tissue damage.

Furthermore, the movement of a stiff needle-electrode array in soft brain tissue enlarges the damaged area or "kill zone". The mechanical mismatch between a stiff needle array and soft brain tissue can be resolved by using flexible materials as the needles. Fernandez et al. have fabricated a SU-8 based flexible needle and demonstrated that a flexible needle can reduce tissue damage[3]. In addition to SU-8, parylene[4] and polyimide[5] are candidate materials for flexible needle electrodes. Consequently, tissue damage can be reduced by (i) minimizing the needle diameter (or cross-sectional area)[10,11] and/or (ii) employing flexible materials in the needle body to follow the tissue's movements[3–5].

To realize very fine flexible needle-electrodes, we have proposed a microneedle array fabricated by selective vapor–liquid–solid (VLS) growth of a silicon wire[13]. In the VLS process, patterning the catalysts can precisely control the diameters and positions of the needles, providing batch fabrication of hundreds or thousands of needles to construct a three-dimensional multiple needle array. Moreover, these needles can be fully integrated with the metal oxide semiconductor (MOS) process for high performance on-chip electronics configurations[14–16].
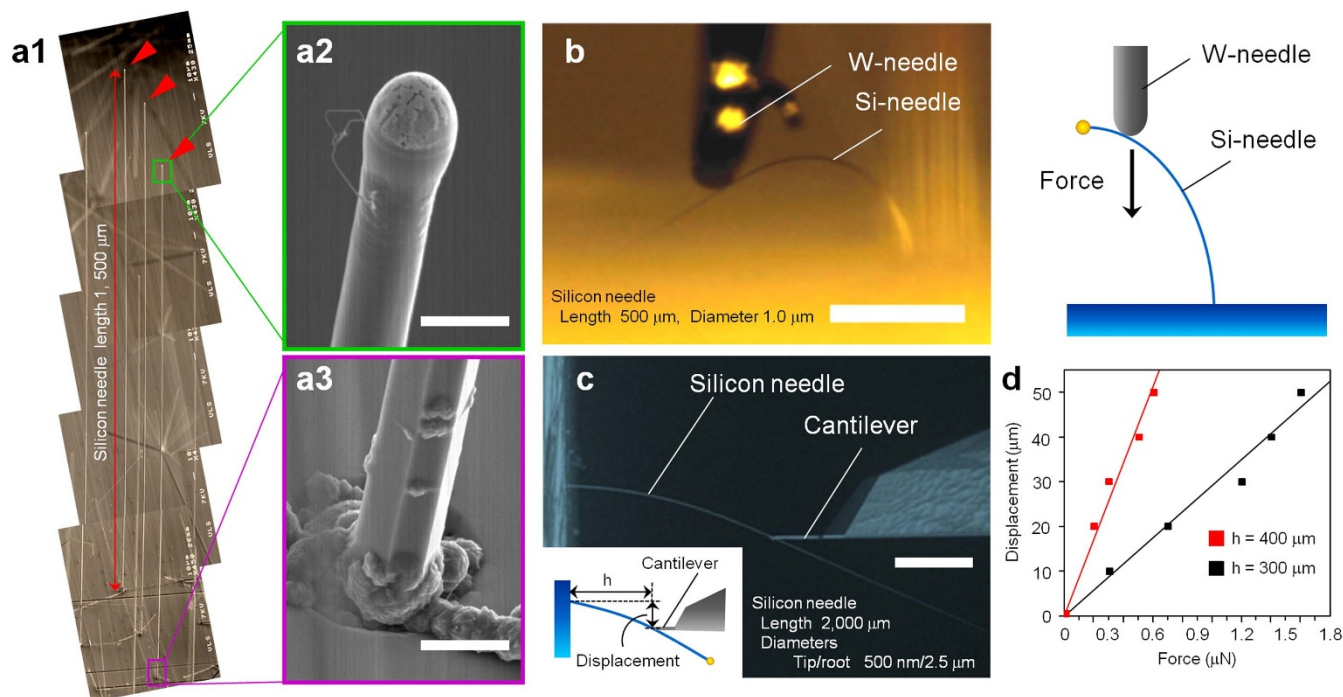
Figure 1 | Silicon microneedles with a high-aspect ratio fabricated by Au-catalyzed vapor–liquid–solid growth of silicon. (a) SEM image of 1,500-μm long silicon microneedles (a1) [(a2) tip and (a3) bottom of a silicon needle]. Scale bars: 3 μm (a2) and 5 μm (a3). (b) Photograph and schematic of a silicon needle (500-μm long and 1-μm diameter) bent with a tungsten needle. Silicon needle exhibits excellent flexibility and robustness when an external force is applied at the needle tip. Scale bar: 200 μm. (c) Quantitative bending tests on a 2,000-μm long silicon microneedle (500-nm tip diameter and 2.5-μm bottom diameter) using a force measurement setup inside a SEM. Scale bar: 100 μm. (d) Displacement-force curves taken from different two measurement points (length h = 300 μm and 400 μm) using the same silicon needle shown in (c).

This methodology allows silicon needles to be fabricated with diameters from the submicron to micron scale. Bending tests of VLS-silicon needles with sub-micron diameters confirm that thinner VLS-grown silicon needles exhibit flexible properties[17,18].

Using a selective VLS silicon growth technique, we have fabricated 3.5-μm diameter, 40-μm long needle-electrode arrays with enlarged 10-μm diameter gold (Au) tips, and confirmed the recording capability of light-evoked responses from a fish retina[19]. However, only the field potentials of neurons, and not the action potentials, were detected[19] because the neuronal action potentials, which included higher frequency components compared to field potentials[20,21], were attenuated more than field potentials by a parasitic low-pass filter (~100-Hz cutoff frequency). The properties of the low-pass filter were induced by the high impedance of each electrode (>1 MΩ at 1 kHz in saline) and the embedded parasitic capacitances of the recording system. Furthermore, the 40-μm long needle is insufficient to reach neurons in deeper layers of the tissue. Hence to record the action potentials of neurons in the cerebral cortex with our microneedle-electrode, the electrode impedance should be reduced[19], and the needle length should be long enough to reach neurons from the cortical surface.

As a step toward a future microneedle-array device for multisite recordings *in vivo*, herein we clarify the penetrating and recording capabilities of individual needles by measuring the mechanical and electrical characteristics of the needles and demonstrating acute *in vivo* action potential recordings. We fabricated flexible needle arrays longer than 210 μm, and improved the higher frequency electrical characteristics of the recording system by reducing the electrode impedance. Specifically, these longer needles were fabricated by controlling the VLS growth parameters and were functionalized as an electrode array by subsequent microfabrication processes for the three-dimensional needles with a high-aspect ratio. The bending tests demonstrated the flexibility of the fabricated needle arrays.

The electrode impedance was reduced by electroplating platinum black (Pt black), although many candidate materials have been reported [e.g., carbon nanotubes[22], iridium oxide (IrOx)[23], and Pt black[24,25]]. Finally, we confirmed the penetration and recording capabilities of the fabricated needle-electrode array by *in vivo* recordings of the neuronal activities from whisker barrel cortical areas of rats.

Results

Mechanical characterizations of VLS-grown silicon microneedles. To reduce tissue damage, an important characteristic of a needle-electrode is flexibility[3–5]. As confirmed by the needle bending tests (Fig. 1), the VLS-grown silicon needles with a microscale diameter were flexible. Figure 1b shows a photograph and schematic of a silicon needle (500-μm long and 1-μm diameter) bent with a tungsten needle. The silicon needle exhibited an excellent flexibility and robustness without fracturing when an external force was applied at the needle tip. We also conducted quantitative bending tests on a 2,000-μm long silicon microneedle (tip diameter of 500 nm and bottom diameter of 2.5 μm) using a force measurement system (FMS) setup inside a scanning electron microscope (SEM) (Fig. 1c). Figure 1d shows the displacement-force curves for the same silicon needle (Fig. 1c) taken from two different measurement points (length h = 300 μm and 400 μm).

Integrated very fine microneedle-electrode array. The VLS-grown silicon microneedles were functionalized as a needle-electrode array for *in vivo* recordings by subsequent microfabrication processes. After growing a needle, the needle-tip was metalized with platinum (Pt) (Figs. 2a–2c). Each fabricated needle device had a linear array of 11 needles spaced at 300 μm intervals (Fig. 3a). This spacing was designed to record the neuronal signals from the whisker barrel area of a rat (~300 μm in diameter for each barrel). Placing the array to the edge of a silicon chip could confirm needle penetration using a

2
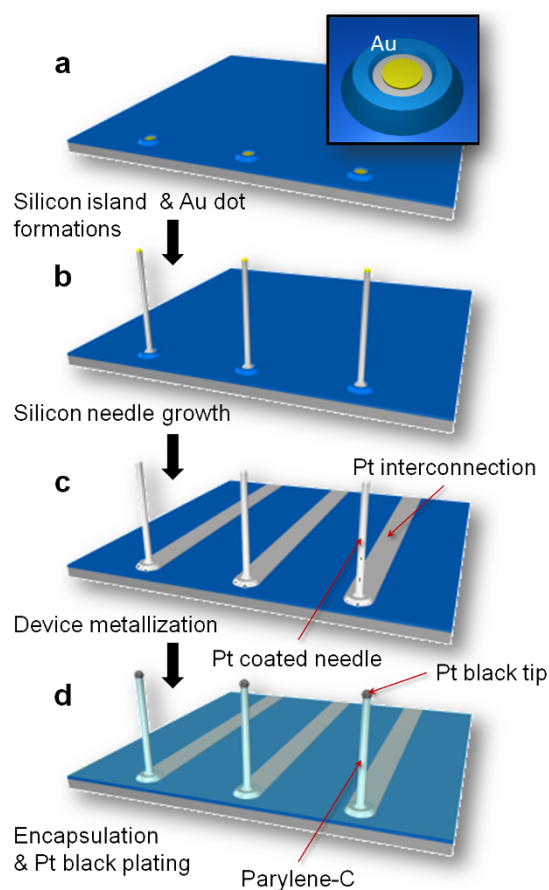
Figure 2 | Schematics for device fabrication. (a) Formation of silicon islands and preparation of catalytic-Au dots. (b) Au-catalyzed VLS growth of silicon needles. (c) Silicon needle metallization and formation of electrical interconnections by sputtering of Pt/Ti and a lift-off process. (d) Device encapsulation with an insulating layer of parylene-C. Tip section of the needle is exposed from the parylene-shell by a plasma process. After tip exposure, the Pt tip is electroplated with Pt black to realize low electrolyte/electrode interfacial electrical impedance characteristics.

microscope. The needle-electrode array was encapsulated with an insulating layer of parylene-C, while the needle tips exposed from the insulator were plated with Pt black (Fig. 2d and Methods). Each needle exhibited a circular-cone shape and a length of 210 μm (Fig. 3b). The tip and base diameters of the needle electrodes before plating with Pt black were 3 μm and 12 μm, respectively.

Electrical characteristics. We fabricated needle-electrodes with various electrode impedances by changing the plating time [0 s (original), 15 s, and 25 s]. The original Pt tip had a diameter of 1.8 μm, but plating times of 15 s and 25 s resulted in Pt black tips with diameters of 4 μm and 7 μm, respectively. Figures 3c and 3d show SEM images of the original and the 25-s Pt black-plated tip, respectively. Pt black plating enlarged the effective recording area at the needle tip, reducing the electrode impedance in saline. Figures 4a and 4b show the dependencies of the magnitude and phase characteristics of the electrode impedance on the Pt black-plating time, respectively. Pt black plating decreased the magnitude of the electrode impedance and shifted the phase angle from the capacitive phase to the resistive phase.

The output/input (O/I) signal ratios of these needle electrodes were measured in saline using test signals of 80 $μV_{p-p}$ sinusoidal waves at frequencies swept from 40 Hz to 7 kHz (see Methods). The O/I ratio increased as the Pt black-plating time increased ("Experiment" in Fig. 4c), indicating that Pt black plating decreased the needle-electrode impedance and increased the O/I ratio (Figs. 4a and 4c). The Pt black-tipped needle-electrode prepared with a maximum plating time of 25 s exhibited an O/I signal ratio of 97% at 1 kHz, whereas the original Pt-tipped needle-electrode displayed a lower ratio of 67% due to the high needle-electrode impedance (Z_e) and the embedded parasitic impedances (C_{line}, C_a, and R_a) in the recording system[19] (see Supplementary Text and Fig. S1c). The phase delays of the recording system with the 25-s Pt black-tipped needle-electrode were less than two degrees from 40 Hz to 7 kHz ("for 25 sec" in Fig. 4d). The O/I signal ratios and phase delays of the needle electrodes measured with the test signals could be described by the equivalent circuit model (Supplementary Fig. S1c) and the measured impedances (Z_e, C_{pa}, and C_{oxide}) (Supplementary Text). The calculated characteristics of both the O/I signal ratios and phase delays ("Calculation" in Figs. 4c and 4d) agreed well with the measured results ("Experiment" in Figs. 4c and 4d).
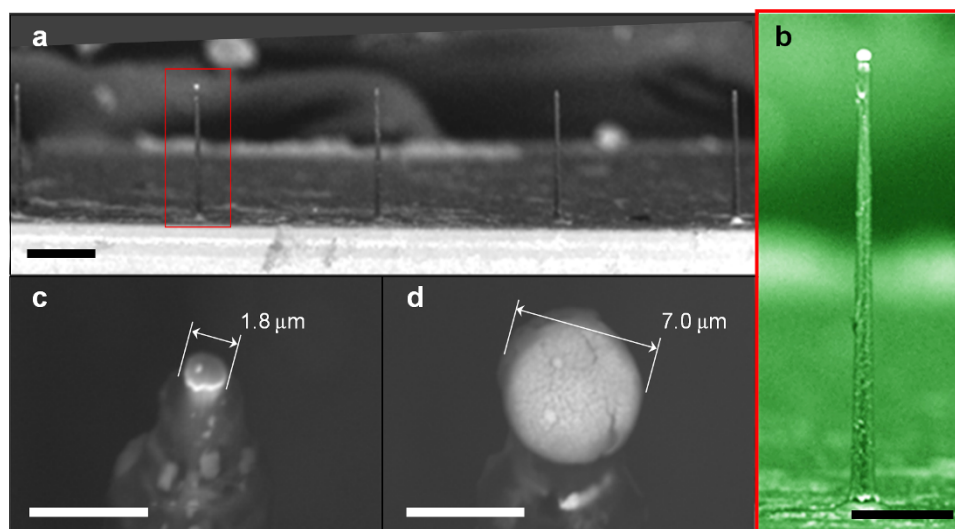
Figure 3 | Fabricated microneedle electrodes by silicon wire growth technology and microfabrication processes. (a) SEM image of an array of needles. Each needle site is 300-μm apart. (b) SEM image of a 210-μm long needle. (c), (d) SEM images of needle tips before (c) and after (d) Pt black electroplating. SEM images (a, b, and d) are consistent with the device used in all the neuronal recordings discussed in this paper. Scale bars: (a) 100 μm, (b) 50 μm, (c) 5 μm, and (d) 5 μm.
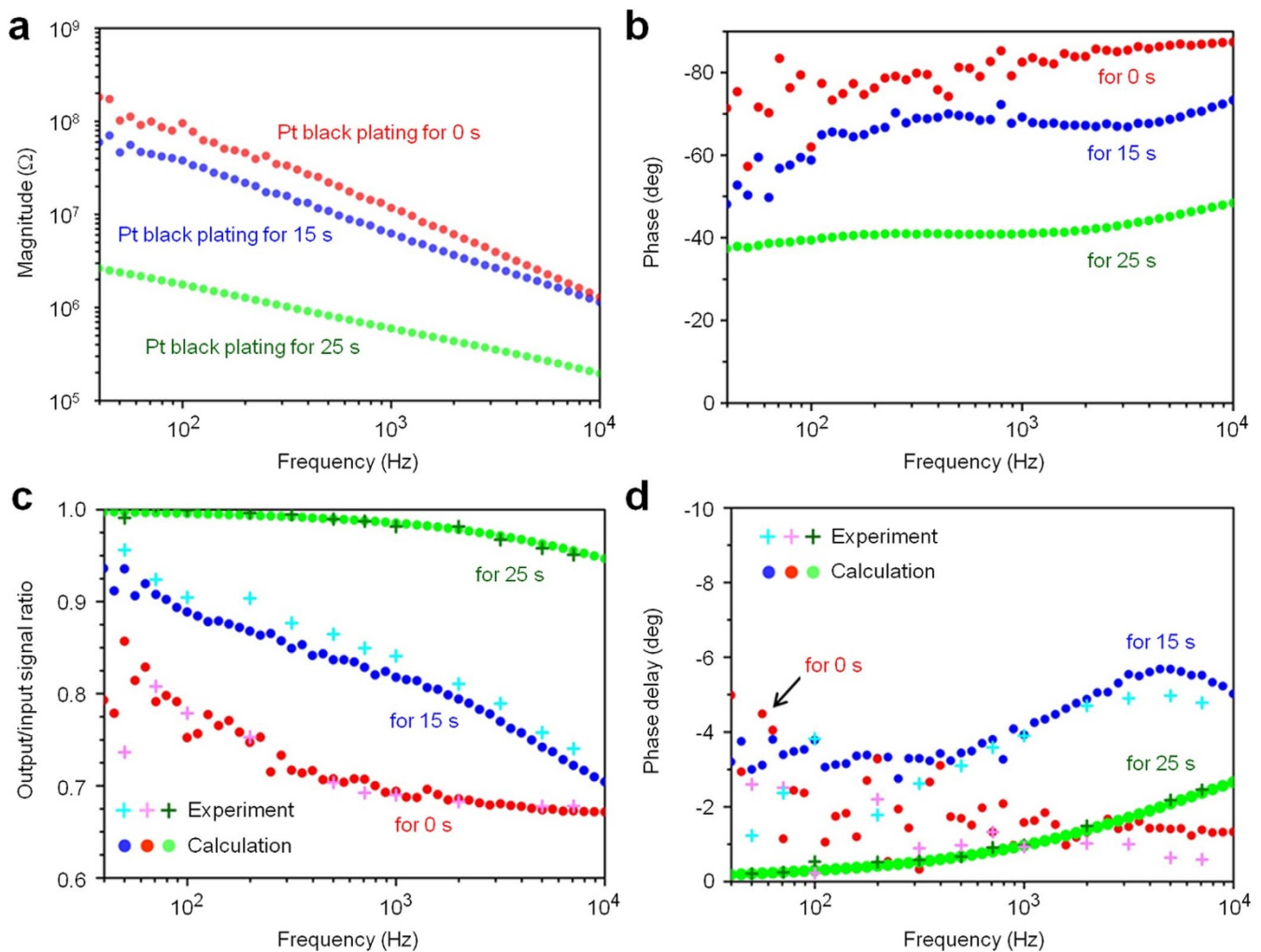
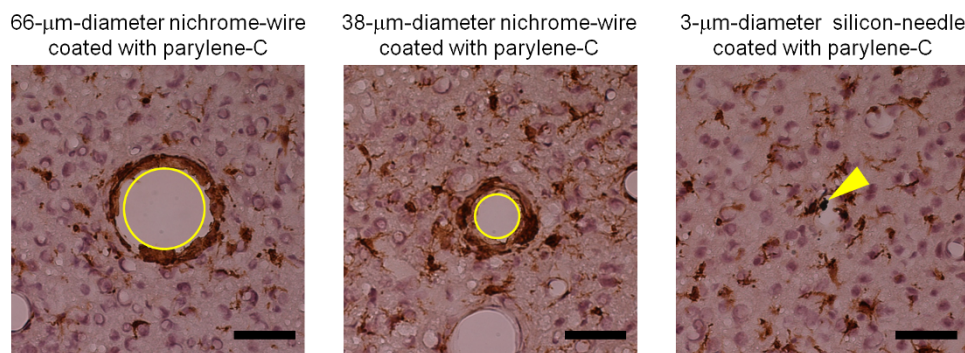**Figure 4 | Electrical properties of microneedle electrodes measured in saline.** (a) Magnitude and (b) phase of electrical impedances of the microneedle electrodes acquired in a room temperature 0.9% NaCl saline solution bath at frequencies from 40 Hz to 10 kHz as functions of the Pt black-electroplating time. (c) Output/input signal amplitude ratios and (d) phase differences of these three needle electrodes taken from test signal recordings. Test signals of 80 μV_{p-p} sinusoidal waves at 40 Hz to 7 kHz are applied to the solution bath. Red, blue, and green circles in (a–d) represent the original Pt tip (without Pt black electroplating), 15-s plated Pt black tip, and 25-s plated Pt black tip, respectively. For comparison, the bottom graphs (c, d) include both calculated (●) and experimental (+) data.

***In vivo* recording.** Animal experiments confirmed the penetration and neural-recording capabilities of the fabricated microneedle electrodes by using needle electrodes. Using two sets, where each set contained an amplifier and a filter, we simultaneously recorded the signals from two electrodes. A total of seven penetrations were performed using two rats. In all penetrations, mechanical stimulation of the principal whisker evoked neuronal activity. Figures 5b–5d show photographs and the recorded signals from the two-channel needle electrode (Chs. 1 and 2 with the interval of 1.5 mm) before and after the needle penetration. In the initial position where the tips of the two needle electrodes were in contact with the cortical surface (the displacement of the manipulator, Z, was 0 μm), wideband signals (15 Hz–10 kHz, see Methods) in response to whisker stimulation were repetitively observed ~20 ms after stimulation (Fig. 5c2). These responses were larger at the Ch. 2 needle electrode than the Ch. 1 needle. Narrowband signals (500 Hz–10 kHz, see Methods) exhibited a small amplitude ranging from −46.9 μV to 46.4 μV [root-mean-square (rms): 6.74 μV_{rms}]. However, upon penetrating the cortex at a depth of $Z = 200$ μm (i.e., the needle-electrode tips were in the shallower part of layers II–III), both the narrowband and wideband signals repeatedly responded to the stimulation and appeared at the Ch. 2 needle electrodes (Fig. 5d2).

After penetration, spike-like waveforms (duration for ~1 ms) were repeatedly observed in the recorded narrowband signals at Ch. 2. These signals ranged from −222.0 μV to 198.4 μV (8.93 μV_{rms}). The waveforms, which consisted of a negative and subsequent positive peak, were subtracted from the original signals using a template matching procedure in the spike-sorting algorithm (see Methods). After subtracting the waveforms, small residual signals at Ch. 2 remained with amplitudes ranging from −54.3 μV to 41.7 μV (7.69 μV_{rms}). Note that the amplitude range of the residual signals was similar to that of the narrowband signals observed prior to needle penetration [−46.9 μV to 46.4 μV (6.74 μV_{rms})], suggesting that the spike-like waveforms could be subtracted from the original waveforms by the template matching procedure. Additionally, the spike-like waveforms observed at Ch. 1 were detected by the template matching procedure. Thus, the detected waveforms were used for further analyses. Figure 5e shows the amplitude distribution of the detected spike-like waveforms after penetration ($Z = 200$ μm). The amplitude distribution of the spike-like waveforms was along the X- and Y-axes in the graph, indicating that these waveforms were independent between channels. The spike-like detected waveforms were classified into three apparent clusters: #14 (the number of waveforms, n = 109), #67 (n = 34), and #87 (n = 136) (Fig. 5e). Figure 5f
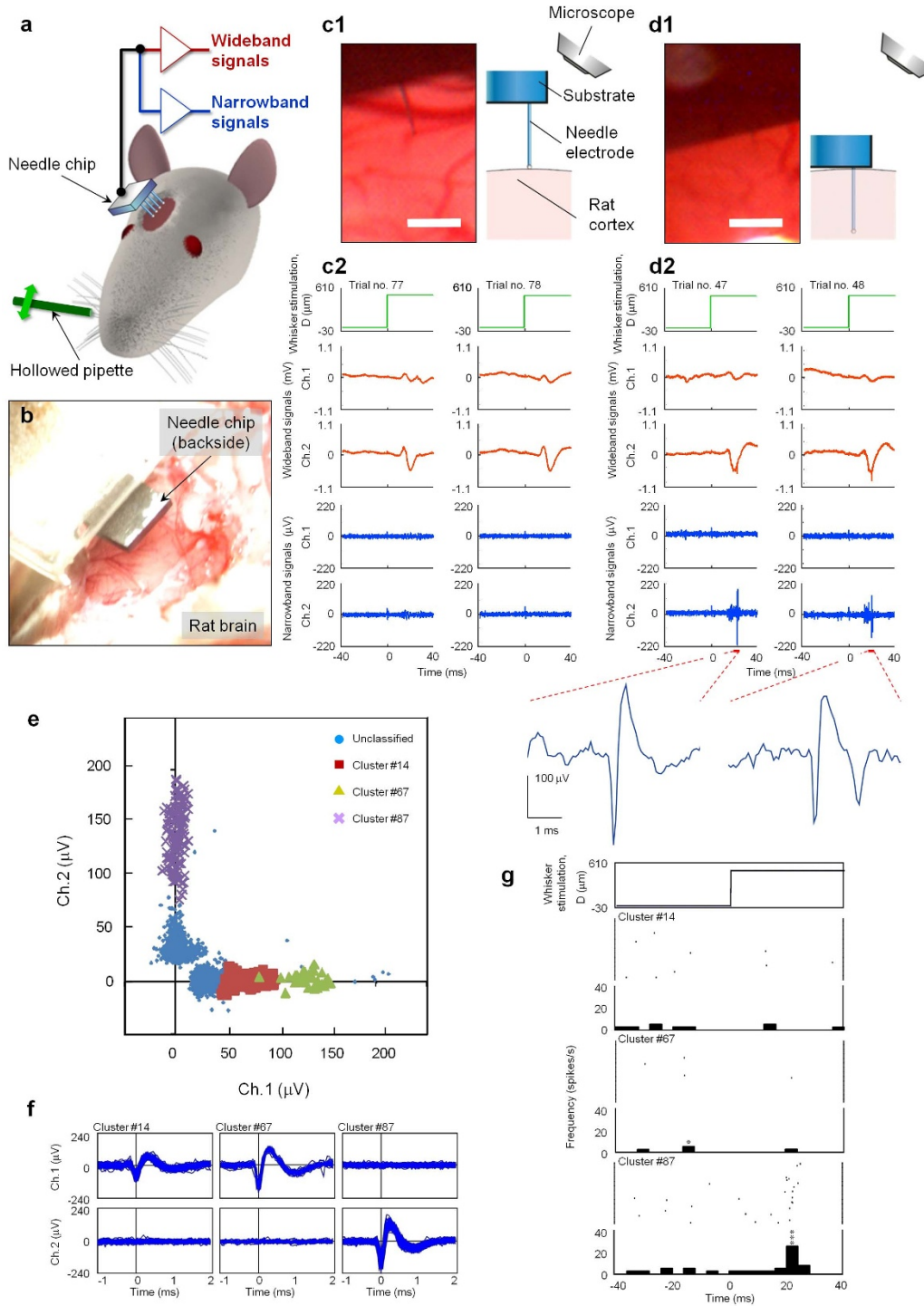
Figure 5 | *In vivo* recording with a needle-electrode array. (a) Schematic of the measurement system. Needle-electrode array penetrates the left whisker barrel area in the somatosensory cortex of a rat. Signals derived from the needle-electrode array are amplified (gain: 2,000) and filtered (bandpass: 15 Hz–10 kHz) to record wideband signals, which are further amplified (gain: 10) and filtered (bandpass: 500 Hz–10 kHz) to obtain narrowband signals. Rat's principal whisker (A1) of the barrel penetrated with a needle-electrode (Ch. 2) is mechanically stimulated with a hollow glass-pipette, and the whisker is deflected with a displacement of 500 μm ["D (μm)"]. Whisker is stimulated at 1 Hz for a 100-s recording period (i.e., 100 trials). (b) Photograph showing the placement of the needle-chip over the cortical surface. (c1, c2) Signals recorded before penetration. (c1) Photograph and schematic show the needle-tip in contact with the cortical surface. (c2) Wideband and narrowband signals derived from two channel needle-electrodes (Ch. 1, Ch. 2) for two successive trials. (d1, d2) Signals recorded after the needles penetrated 200 μm. Explanation of the panels (d1) and (d2) are the same as that in (c1, c2). Panel (d2) also includes enlarged waveforms of the narrowband signals at Ch.2 ~ 20 ms after whisker stimulation. Scale bars in (c1) and (d1): 200 μm. (e) Amplitude distribution of the spike-like waveforms simultaneously recorded at Ch. 1 and Ch. 2 after needle penetration. Spike-like waveforms are classified into three clusters: orange squares (cluster #14), yellow triangles (#67), and purple crosses (#87). (f) Superimposition of spike-like waveforms included in each cluster: #14 (the number of waveforms, n = 109), #67 (n = 34), and #87 (n = 136). (g) Rasters and peri-stimulus time histograms (PSTHs) of spike-like waveforms in the three different clusters. Uppermost graph shows displacement *D* of the principal whisker in the rostral direction. Other graphs show the rasters and PSTHs of clusters #14, #67, and #87 (Figs. 5e and 5f). Bin width: 4 ms. Asterisk denotes a significant spike; single: p < 0.05 and triple: p < 0.001 (one-sided binomial test assuming equiprobable spike occurrence between bins).

66-μm-diameter nichrome-wire coated with parylene-C

38-μm-diameter nichrome-wire coated with parylene-C

3-μm-diameter silicon-needle coated with parylene-C

Figure 6 | Immunohistochemical evaluation of tissue four days after implantation of nichrome wires and a silicon microneedle. Microglia (brown) and nucleus (violet) are identified with immunohistochemical staining with the Iba1 antibody and the counterstaining with hematoxylin, respectively. Panels show microglia around a 66-μm-diameter nichrome wire (left), a 38-μm-diameter nichrome wire (center), and a 3-μm-diameter silicon needle (right). All of the wires and the needle were coated with parylene-C (thickness of 1 μm). Yellow circles in the left and center panels show traces of the 66-μm-diameter and 38-μm-diameter nichrome wires, respectively. Yellow arrow in the right panel shows the silicon microneedle remaining in the tissue. While the length of the silicon microneedle was 750 μm and those of the nichrome wires were 1 mm, these tangentially sliced sections were sampled at depths between 320 μm and 440 μm from the cortical surface of a rat. Scale bar: 50 μm.

demonstrates that the detected spike-like waveforms classified into clusters were well superimposed. Note that the spike-like waveforms in cluster #14 had smaller amplitudes, and might include misclassifications. Figure 5g shows the rasters and the peri-stimulus time histograms (PSTHs) of the detected spike-like waveforms of the three apparent clusters. The probability of the spike-like waveforms appearing in cluster #87 was higher in the 4-ms bin of 24 ms after mechanical stimulation of the principal whisker in the rostral direction, suggesting that these spike-like waveforms were evoked by whisker stimulation.

Immunohistochemical analysis. Hemorrhaging and ischemia after electrode needle penetration cause cerebral injury following immune reactions of glial cells. Here we demonstrate that reducing the needle diameter minimizes tissue damage. Glial cells are known to change their activities after a traumatic cerebral injury. In particular, microglia are activated and concentrated in the damaged area. We evaluated such immune reactions after needle penetration [3-μm-diameter silicon needle (750 μm in length), 38-μm-diameter nichrome wire (1 mm in length), or 66-μm-diameter nichrome wire (1 mm in length)]. Figure 6 shows the distributions of microglia, which were identified with the calcium-binding protein Iba1, around the needles four days after implantation. The tangentially sliced sections were sampled at depths between 320 μm and 440 μm from the cortical surface. The nichrome wires were removed before slicing the tissue, but the silicon needle was not. Because the silicon needle could be cut during tissue slicing, referring to the piece easily identified the needle penetration position. In Fig. 6, the yellow arrow shows the silicon-needle position (right panel), while circles denote the traces of the nichrome wires (left and middle panels). Although all the needles were surrounded by microglia, fewer microglia surrounded the silicon needle. Furthermore, comparing the morphological difference of microglia between the photos in Fig. 6, the microglia near the silicon needle exhibited a ramified form, but those surrounding nichrome wires did not. Because microglia are activated after injury and concentrate at the injury site[26] by morphologically changing their shape from the ramified form to the phagocytic form[27], these results suggest that reducing the needle diameter can minimize the immune reaction.

Discussion

Herein we fabricate a very-fine three-dimensional needle-electrode array, which is longer than 210 μm. Bending tests confirm the high flexibility (Fig. 1), and the results indicate that the curves obey the formula for displacement δ,

$$\delta = \frac{2}{3\pi} \frac{WL^3}{Er^4},$$

where W denotes the external force by FMS. L, r, and E are the length, radius, and Young's modulus (188 GPa for <111> silicon needle by VLS growth) of the needle, respectively. The formula also indicates that the displacement per force (δ/W), which represents the flexibility, proportionally increases with $1/r^4$. This suggests that our silicon needle with a microscale radius and diameter is more flexible than other silicon-microelectromechanical systems (MEMS)-based needles with larger diameters (approximately tens of microns) and cross-sectional areas. Assuming that the silicon needle is a conventional electrode with a diameter of 50-μm, a length of 1.5 mm, and Young's modulus of 130 GPa (<100> silicon needle), the displacement per force (δ/W) is 0.014 mN^{-1}. Using this formula gives $\delta/W = 3810$ mN^{-1} for our silicon needle (diameter = 2 μm, length = 1.5 mm, and Young's modulus = 180 GPa), indicating that our needle is 2.7×10^5 times more flexible than a 50-μm diameter silicon needle. Because our 210-μm silicon microneedles can penetrate into a rat's cerebral cortex as demonstrated in the *in vivo* recording (Fig. 5), the fabricated 210-μm-long needle-electrode has a sufficient longitudinal stiffness to punch a tissue. However, a further discussion of tissue penetration using longer needles (>210 μm) is necessary because higher aspect-ratio silicon needles should reduce the longitudinal stiffness of the needle itself, resulting in buckling or fracturing of the needle prior to penetration.

Our previous microneedle arrays[19] have enabled the field potentials of neural activities to be recorded, but not the neuronal action potentials, because the high needle-electrode impedance (Z_e) and embedded parasitic impedances (C_{line}, C_a, and R_a) in the recording system attenuated the detected neural activities[19] (see Supplementary Text and Fig. S1). To prevent attenuations, the electrode impedance should be reduced or the embedded parasitic impedances should be increased. However, to realize an electrode array applicable to numerous recording systems, which have a variety of embedded impedances, the reduction in the electrode impedance must be an appropriate strategy. Thus, we modified the tips of the microneedle electrodes using Pt black, which is a low impedance material. The Pt black-tipped needle electrode exhibits a sufficiently low-impedance with a high O/I ratio characteristic for use in neuronal spike recordings.

In the experiments with different electroplating times, the O/I signal ratio increases as the electroplating times increases for high impedance needle electrodes (Fig. 4c). High impedance needle-

electrodes with the original Pt tip and 15-s plated Pt black tip exhibit lower O/I signal ratios (<85%) at higher frequencies (>1 kHz). Because the neuronal action potentials consist of higher frequency components compared to the field potentials, the action potentials recorded with high impedance electrodes are attenuated more. These observations are consistent with our previous findings where a high-impedance needle electrode (more than 1 MΩ at 1 kHz in saline for a 10-μm diameter Au tip) with parasitic capacitances embedded in the recording system only detects the field potentials of fish retina [electroretinogram (ERG), ~500 Hz][19]. The findings herein indicate that the high impedance characteristics of the electrode limit the miniaturization of the electrode to record neuronal action potentials. However, selectively modifying the electrode tips with a low impedance material such as Pt black can resolve this issue (Figs. 2d and 3d). These modified electrode tips should further reduce the diameter of the needle electrode (<3 μm) and realize a submicron needle electrode, opening a new class of electrophysiology such as sub-microscale stimulations and recordings of neurons in vivo [an in vitro application of nanoelectrode arrays has been demonstrated[28]].

Microneedle electrodes with Pt black-electroplated tips exhibit negligible changes in their electrical and mechanical properties before and after in vivo cortical recordings. Indeed, the impedance of a needle extracted from a rat's cortex after recording for more than three hours is 640 kΩ at 500 Hz, which is similar to that of the same needle prior to cortical penetration (600 kΩ at 500 Hz). We also observed the SEM images of needles after extraction from the cortex and confirmed that neither the Pt black tip nor the needle body sustained significant damage. Figures 3a, 3b, and 3d show SEM images acquired after cortical extraction of the needle array, which was used in all the in vivo cortical recordings discussed in this paper (Fig. 5).

Animal experiments confirm the penetration and neural-recording capabilities of the fabricated microneedle electrodes. Both before (Fig. 5c1) and after (Fig. 5d1) penetration of the two-channel microneedle electrodes into the whisker barrel area of a rat, the wideband signals at Ch. 2 are clearly deflected ~20 ms after whisker stimulation (Figs. 5c2 and 5d2), while those at Ch. 1 have smaller deflections. During the recordings, these deflections of the wideband signals at Ch. 2 repetitively appear with a latency of ~20 ms and have similar waveforms. Because the latency and waveform are similar to those of the rats' field potentials in previous studies[20,21], these wideband signals are referred to as local field potentials induced by whisker stimulation.

Deflections of the narrowband signals, which are the higher frequency components of the wideband signals (see Methods), are insignificant prior to needle electrode penetration (Fig. 5c2), but are larger at Ch. 2 after a 200-μm penetration (Fig. 5d2), indicating that some high frequency components appear after the 200-μm penetration. Such high frequency components can be separated into spike-like waveforms using a template matching method (see Methods). Because no remarkable deflections remain after the detected spike-like waveforms are removed, the high frequency components present after electrode penetration are composed of the detected spike-like waveforms. The detected spike-like waveforms are local signals because they appear independently between Ch. 1 and Ch. 2 (Figs. 5d2, 5e, and 5f)[29,30].

The detected spike-like waveforms can be classified into several types: those under the noise level and those in clusters #14, #67, and #87. Clusters #67 and #87 are especially concentrated at the centers and are well separated from the other clusters (Fig. 5e). Additionally, their spike-like waveforms are superimposable (Fig. 5f), indicating that similar waveforms appear repetitively in an all-or-nothing manner. Although these two types of superimposed waveforms have different amplitudes, durations, and observed channels, they have a common waveform pattern, i.e., a large negative deflection, as shown at Ch. 1 for cluster #67 and at Ch. 2 for cluster #87 (Fig. 5f).

This common waveform pattern is consistent with the typical waveform of neuronal action potentials in extracellular recordings using conventional microelectrodes where the waveform has a negative potential deflection and a duration of ~1 ms[31,32].

Due to the aforementioned features of the detected spike-like waveforms [i.e., spatial localization, occurrence in an all-or-nothing manner, and a similar waveform as neuronal action potentials[29,31,33]], the detected spike-like waveforms are consistent with neuronal action potentials. As additional evidence, we demonstrated that the spike-like waveforms in a cluster occur synchronously with certain events, indicating that the presence of the spike-like waveforms provides information about the events. The appearance probability of the spike-like waveforms in cluster #87 increases ~25 ms after stimulating the principal whisker (Fig. 5g). Thus, the spike-like waveforms of cluster #87 are related to principal whisker stimulation, i.e., event related, while the other classified waveforms (#14 and #67 clusters) are activities related to other events or spontaneous activities. Consequently, the spike-like waveforms included in the narrowband signals are neuronal action potentials, indicating that in vivo neuronal action potentials can be recorded by our microneedle-electrode arrays.

Because we successfully demonstrated that minimizing the needle diameter reduced tissue damage, our silicon-needle arrays may decrease tissue damage. Cerebral ischemia and intracerebral hemorrhage are the main causes of the cerebral damage after needle penetration. Microglia are known to play an important role in the early stage of the cellular reactions (i.e., migrating and concentrating in the damaged area). Thus, we immunohistochemically evaluated the distribution of microglia four days after penetration of needles with different diameters. The thinner silicon needle shows fewer signs of microglia reactions than the thicker needles, suggesting that penetration with a thinner needle causes less tissue damage. Such cellular reactions to evaluate penetration damage have been studied with not only microglia but also other cells in the brain[11,34]. Szarowski et al. reported tissue damage in rats' brain due to implantations of different types of microscale needles by investigating astrocytes and microglia for ~12 weeks[11]. They demonstrated that the volume of the reactive tissue involved in the early stage (i.e., <1 week) is proportional to the cross-sectional area of implanted needles. Kozai et al. reported that penetration of ~8.5-μm-diametercarbon-fiber electrode (~7-μm-diameter carbon fiber with an ~800-nm-thick poly(p-xylylene) insulator layer) causes tissue damage in a rat's brain by investigating the reactions of astrocytes, microglia, endothelial cells, and neurons two weeks after implantation[34]. Their results suggest that such small implantable needles can reduce tissue responses induced by penetration. Furthermore, in chronic in vivo recording experiments over five weeks in the cerebral cortex, they reported that the probability of detecting neuronal action potentials with carbon-fiber electrodes was higher than with other conventional electrodes, suggesting that less invasive electrodes elongate the recordable period of neuronal signals. Although further studies are necessary, our histological data (Fig. 6) as well as the aforementioned studies suggest that our silicon needles have potential for use in not only acute but also chronic neuronal recordings with less nervous tissue damage.

In summary, we had previously investigated the electrical characteristics of a microscale needle electrode and found that the needle electrode exhibits high impedance characteristics and low O/I signal ratios due to the small recording area at the tip section. In addition to the electrical properties, a 40-μm-long needle was insufficient for in vivo recordings of neuronal action potentials. To realize in vivo recordings of neuronal action potentials using microneedles, we fabricated 210-μm-long Pt black-tipped microneedle-electrode arrays, which exhibit low needle-electrode impedances and high O/I signal ratio characteristics in saline. In addition to confirming the penetration capability of the needle array, we demonstrated that a Pt black-modified microneedle-electrode-array chip can record both the

neuronal action potentials and the field potentials of neurons from a rat's whisker barrel area *in vivo*. Thus, VLS-grown-silicon wire-based microneedle-electrode arrays are applicable to *in vivo* recordings of neuronal action potentials. Compared to conventional electrodes with needle diameters of ~100 μm, the clear advantage is that our device with microscale diameter needles reduces the kill zone for *in vivo* action potential recordings. Moreover, these microneedle-electrode arrays are promising in fundamental neuroscience and medical applications as less invasive devices.

Methods

Ethics statement. All experimental procedures using rats adhered to the guidelines of the National Institutes of Health of the United States in 1996 and the Japan Neuroscience Society. The institutional committee for animal experiments at the National Institute of Advanced Industrial Science and Technology approved the experimental protocols.

Fabrication of a very fine needle-electrode array. A three-dimensional microscale needle-electrode array was fabricated on a silicon substrate by a selective VLS-silicon growth-based process (Fig. 2). Due to the VLS growth mechanism, <111>-oriented silicon microneedles were grown and assembled perpendicular to the silicon-(111) substrate, realizing a suitable design for a three-dimensional penetrating needle-electrode array with numerous needles and a high spatial resolution. After forming interconnections between the needle site and the chip-bonding pad, the device was covered with a biocompatible insulator, and then each needle tip was exposed to form a low impedance material of Pt black by electroplating.

The fabrication process began with a silicon-on-insulator (SOI) substrate, which consisted of a 2-μm thick (111) top silicon (n-type with a resistivity of 0.02 Ω·cm) layer, a 2-μm thick buried oxide layer, and a 520-μm thick handle silicon substrate. The top silicon layer served as a platform for the VLS-silicon needle-electrode array, and an array of 20-μm diameter silicon islands was formed by reactive ion etching (RIE). The substrate, including silicon islands, was subsequently covered with a silicon dioxide (SiO_2) layer by oxidizing the substrate. Then the SiO_2 layer on the center of each silicon island was etched away, exposing the island surface for the subsequent VLS growth. Over the exposed silicon surface of each island, evaporation and subsequent photoresist-based lift-off processes placed a catalytic-Au dot (200-nm thick) (Fig. 2a).

VLS growth of silicon with a catalytic-Au dot could assemble out-of-plane very-fine needles. The substrate was set in a gas source-molecular beam epitaxy (GS-MBE) chamber, and then Au-catalyzed VLS growth of silicon was conducted to grow individual silicon needles from the islands (Fig. 2b). Herein, disilane (Si_2H_6) was the silicon gas source at a gas pressure of 0.55 Pa and a growth temperature of 700°C[35]. The needle length was precisely controlled at a constant needle growth rate of 1.16 μm/min. After fabricating the needles, a multiple layered metal system of Pt/titanium (Ti) (thicknesses = 50/20 nm) was formed by repeated sputtering and lift-off processes to ensure needle metallization as well as the interconnection between the needle site and the bonding pad (Fig. 2c).

The overall substrate was then covered with a biocompatible device insulator [1.4-μm thick parylene-C layer (model PDS2010, LABCOTER)]. Finally, inductively coupled plasma RIE (ICP RIE) with an oxygen plasma exposed the Pt needle-electrode tip to be used as the recording site. During the RIE process, other parylene sections of the sidewall of the needle electrode and the substrate surface were protected with an additional photoresist film.

Pt black plating. To achieve a sufficiently low needle-electrode impedance for use in neural recordings, the Pt tip of the needle electrode was selectively electroplated with Pt black (Fig. 2d). Herein the plating solution consisted of Pt chloride containing 10 g $H_2PtCl_6\cdot6H_2O$, 0.1 g $Pb(CH_3COO)_2\cdot3H_2O$, and 300 mg diluted water[24]. We used a negative voltage (−400 mV) for each Pt-tipped needle-electrode for the device in the plating solution, while a Pt-wire in the solution was used as the counter electrode. The plating time was either 0 s, 15 s, or 25 s in order to investigate the effect of plating time on the electrical properties of the needle electrode. After plating, the device was immersed in solution (saline) to avoid air bubbles forming inside the Pt black sections, which stabilized the impedance characteristics of the needle-electrodes.

Impedance measurements. The needle-electrode impedance was measured in a 0.9% sodium chloride (NaCl) saline solution bath at room temperature by applying a test sinusoidal wave (50 mV$_{P-P}$ amplitude, 10 Hz–10 kHz) via a silver-silver chloride (Ag-AgCl) counter electrode. For all measurements, we used an impedance analyzer (Model 1260A Impedance/Gain-Phase Analyzer, AMETIC, Inc).

O/I signal ratio measurements. The O/I signal amplitude ratios of the recording system were analyzed by applying test signals to a device chip in a saline solution bath[15]. Herein 80 μV$_{P-P}$ input sinusoidal wave signals (40 Hz–7 kHz) were applied to the solution bath via a Ag-AgCl electrode. The input signals were amplified by a pre-amplifier and a main-amplifier (gain: 20,000, filtering: 15 Hz–10 kHz; AB-610J, Nihon Koden, Japan).

In vivo neural recording. *In vivo* needle-electrode penetrations and neural recordings were carried out on the sensory cortex of two male Sprague-Dawley rats (383 g-weight and 385 g-weight). The needle-electrode array penetrated the whisker barrel area in the somatosensory cortex, and signals induced by stimulating the principal whisker of the barrel area were recorded via the needle electrodes (Fig. 5a).

In this experiment, a deeply anesthetized rat was fixed in a stereotaxic instrument using ear-bars while the body temperature was maintained at 37°C with a thermostatically regulated heating pad. The skull over the whisker barrel area in the left hemisphere was opened by a craniotomy. After removing the dura, the needle-electrode array was inserted into the barrel area. A rat's stainless steel mouthpiece served as the reference electrode. The chip of the needle electrodes mounted on an x-y-z micromanipulator system was positioned over the left whisker barrel area with the needle side facing down (Figs. 5a and 5b). The needle array was inserted into the barrel area by controlling the manipulator, while signals induced by whisker stimulation were monitored via the measurement system (Figs. 5c and 5d). The signals were recorded through biological amplifiers and filters (gain: 20,000, filtering: 500 Hz–10 kHz for narrowband signals; gain: 2,000, filtering: 15 Hz–10 kHz for wideband signals). While monitoring the narrowband signals via the Ch. 2 electrode, the principal whisker, which is the whisker with the maximum signal induced by manual whisker deflections, was determined. After the electrode was retracted, the end of the principal whisker was inserted into a hollowed pipette whose end was fixed to a piezoelectric actuator (Fig. 5a). The piezoelectric actuator was repetitively deflected in the caudal-to-rostral direction with a displacement (e.g., 500 μm) at 1 Hz [interval: 500 ms, 100-s recording period (i.e., 100 trials)]. Then the needle-chip was precisely moved downward to reach the surface of the barrel area by controlling the manipulator. Signals induced by the whisker stimuli were recorded via Chs. 1 and 2 before (the initial position of the needle electrodes: Z = 0 μm) and after (Z = 200 μm) penetration into the whisker barrel area. To realize stable impedance characteristics of the needle-electrodes, the needle-tips were not allowed to dry.

Waveform analysis for narrowband signals. Waveforms of the narrowband signals were analyzed by a spike-sorting algorithm for multichannel recording data. The algorithm was developed and used to detect and classify neuronal action potentials recorded from a conventional multichannel microelectrode [see details in[29,32]]. Briefly, the spike-sorting algorithm consisted of four procedures: spike detection, spike vectorization, burst detection, and spike classification. Spikes were detected by matching the recorded waveforms with a set of spike templates with different durations (spike detection). The amplitudes of the spike waveforms simultaneously recorded at different sites constituted a vector (spike vectorization). Burst firings of neurons were detected based on the attenuation of the spike amplitude and on the interspike intervals (burst detection). Finally, clusters of spike-amplitude vectors were statistically classified by bottom-up hierarchical clustering (spike classification). Note that the spike-sorting algorithm was used as an analysis method, and waveform analysis by the algorithm did not necessarily indicate that the waveforms detected as spikes were generated from neurons. The relationship between the detected signals and neuronal action potentials is discussed in the main text (see Result and Discussion).

Immunohistochemical analysis. We assessed microglial activation to immunohistochemically evaluate tissue damages after needle penetration [3-μm-diameter silicon needle (750 μm in length), 38-μm-diameter nichrome wire (1 mm in length), or 66-μm-diameter nichrome wire (1 mm in length)]. All the needles were coated with a 1-μm-thick layer of parylene C. Under an anesthetized surgery, needles were penetrated through slits on the dura mater and implanted in the left cerebral cortex of a male Wistar rat weighing 491 g. The surgical procedure was similar to the acute animal experiments, but the craniotomy hole was covered with dental cement and the skin was sutured at the end of the surgery. Four days after the implantation, the anesthetized rat was perfusion-fixed with 4% paraformaldehyde phosphate buffer solution and the brain was removed. After overnight post-fixation and sucrose cryoprotection, the brain was frozen for sectioning using a cryostat. We removed the nichrome needles before freezing the brain, but left silicon needles as markers. The sections were tangentially sliced (20-μm thick) and immunohistochemically stained using a rabbit polyclonal antibody that binds to a microglia/macrophage-specific calcium-binding protein (Iba1 antibody; BIOCARE Medical LLC, Concord, USA). The protein is specifically expressed in microglial cells and is upregulated during activation of these cells. To visualize the cell nuclei, hematoxylin staining (Hematoxylin QS, H-3404; Vector Laboratories, Inc., Burlingame, USA) was applied as the counterstaining. For negative-control sections, normal rabbit immunoglobulin G (IgG; AB-105-C; R&D Systems, Inc., Minneapolis, USA) instead of the Iba1 antibody was applied to in the primary-antibody-reaction process, and the counterstaining was not performed.

1. Bai, Q., Wise, K. D. & Anderson, D. J. A high-yield microassembly structure for three-dimensional microelectrode arrays. *IEEE Trans. Biomed. Eng* **47**, 281–289 (2000).
2. Rousche, P. J. & Normann, R. A. Chronic recording capability of the Utah Intracortical Electrode Array in cat sensory cortex. *J. Neurosci. Methods* **82**, 1–15 (1997).
3. Fernandez, L. J. *et al.* Study of functional viability of SU-8-based microneedles for neural applications. *J. Micromech. Microeng.* **19**, 025007 (2009).

4. Takeuchi, S., Ziegler, D., Yoshida, Y., Mabuchi, K. & Suzuki, T. Parylene flexible neural probes integrated with microfluidic channels. *Lab Chip* **5**, 519–523 (2005).

5. Rousche, P. J. *et al.* Flexible polyimide-based intracortical electrode arrays with bioactive capability. *IEEE Trans. Biomed. Eng.* **48**, 361–371 (2001).

6. Varney, M. W., Aslam, D. M., Janoudi, A., Chan, H. Y. & Wang, D. H. Polycrystalline-diamond MEMS biosensors including neural microelectrode-arrays. *Biosensors* **1**, 118–133 (2011).

7. Serruya, M. D., Hatsopoulos, N. G., Paninski, L., Fellows, M. R. & Donoghue, J. P. Brain-machine interface: Instant neural control of a movement signal. *Nature* **416**, 141–142 (2002).

8. Hochberg, L. R. *et al.* Neuronal ensemble control of prosthetic devices by a human with tetraplegia. *Nature* **442**, 164–171 (2006).

9. Hochberg, L. R. *et al.* Reach and grasp by people with tetraplegia using a neurally controlled robotic arm. *Nature* **485**, 372–375 (2012).

10. Edell, D. J., Toi, V. V., McNeil, V. M. & Clark, L. D. Factors influencing the biocompatibility of insertable silicon microshafts in cerebral cortex. *IEEE Trans. Biomed. Eng.* **39**, 635–643 (1992).

11. Szarowski, D. H. *et al.* Brain responses to micro-mashined silicon device. *Brain Res.* **983**, 23–35 (2003).

12. Polikov, V. S., Tresco, P. A. & Reichert, W. M. Response of brain tissue to chronically implanted neural electrodes. *J. Neurosci. Methods* **148**, 1–18 (2005).

13. Kawano, T. *et al.* Electrical interfacing between neurons and electronics via vertically-integrated sub-4 micron-diameter silicon probe arrays fabricated by vapor-liquid-solid growth. *Biosens. Bioelectron.* **25**, 1809–1815 (2010).

14. Kawano, T. *et al.* Selective vapor-liquid-solid epitaxial growth of micro-Si probe electrode arrays with on-chip MOSFETs on Si (*111*) *sub*strates. *IEEE Trans. Electron Devices* **ED-51**, 415–420 (2004).

15. Takei, K. *et al.* Integration of out-of-plane silicon dioxide microtubes, silicon microprobes, and on-chip *NMOSFETs by selective vapor*-liquid-solid growth. *J. Micromech. Microeng.* **18**, 035033 (2008).

16. Okugawa, A., Mayumi, K., Ikedo, A., Ishida, M. & Kawano, T. Heterogeneously integrated vapor-liquid-solid grown silicon probes/(111) and silicon MOSFETs/(100). *IEEE Electron Device Lett.* **32**, 683–685 (2011).

17. Hoffmann, S. *et al.* Measurement of the bending strength of vapor-liquid-solid grown silicon nanowire. *Nano let.* **6**, 622–625 (2006).

18. Zhu, Y., Xu, F., Qingquan, Q., Fung, W. Y. & Lu, W. Mechanical properties of vapor-liquid-solid synthesized silicon nanowires. *Nano let.* **9**, 3934–3939 (2009).

19. Harimoto, T. *et al.* Enlarged gold-tipped silicon microprobe arrays and signal compensation for multi-site electroretinogram recordings in the isolated carp retina. *Biosens. Bioelectron.* **26**, 2368–2375 (2011).

20. Gaute, T. E. *et al.* Laminar population analysis: estimating firing rates and evoked synaptic activity from multielectrode recordings in rat barrel cortex. *J. Neurophysiol.* **97**, 2174–2190 (2007).

21. Di, S., Baumgartner, C. & Barth, D. S. Laminar analysis of extracellular field potentials in rat vibrissa/barrel cortex. *J. Neurophysiol.* **63**, 832–840 (1990).

22. Keefer, E. W., Botterman, B. R., Romero, M. I., Rossi, A. F. & Gross, G. W. Carbon nanotube coating improves neuronal recordings. *Nat. Nanotechnol.* **3**, 434–439 (2008).

23. Gawad, S. *et al.* Substrate arrays of iridium oxide microelectrodes for in vitroneuronal interfacing. *Front. Neuroeng.* **2**, 1 (2009).

24. Oka, H., Shimono, K., Ogawa, R., Sugihara, H. & Taketani, M. A new planar multielectrode array for extracellular recording: application to hippocampal acute slice. *J. Neurosci. Methods.* **93**, 61–67 (1999).

25. Heer, F. *et al.* CMOS microelectrode array for the monitoring of electrogenic cells. *Biosens. Bioelectron.* **20**, 358–366 (2004).

26. Davalos, D. *et al.* ATP mediates rapid microglial response to local brain injury *in vivo*. *Nat. Neurosci.* **8**, 752–758 (2005).

27. Thomas, W. E. Brain macrophages: evaluation of microglia and their functions. *Brain Res. Rev.* **17**, 61–74 (1992).

28. Patolsky, F. *et al.* Detection, stimulation, and inhibition of neuronal signals with high-density nanowire transistor Arrays. *Science* **313**, 1100–1104 (2006).

29. Kaneko, H., Tamura, H. & Suzuki, S. S. Tracking spike-amplitude changes to improve the quality of multineuronal data analysis. *IEEE Trans. Biomed. Eng.* **54**, 262–72 (2007).

30. Henze, D. A., Borhegyi, Z., Csicsvari, J., Mamiya, A., Harris, K. D. & Buzsáki, G. Intracellular features predicted by extracellular recordings in the hippocampus in vivo. *J. Neurophysiol.* **84**, 390–400 (2000).

31. Buzsáki, G., Penttonen, M., Nádasdy, Z. & Bragin, A. Pattern and inhibition-dependent invasion of pyramidal cell dendrites by fast spikes in the hippocampus in vivo. *Proc. Natl. Acad. Sci. U. S. A.* **93**, 9921–9925 (1996).

32. Kaneko, H., Suzuki, S. S., Okada, J. & Akamatsu, M. Multineuronal spike classification based on multisite electrode recording, whole-waveform analysis, and hierarchical clustering. *IEEE Trans. Biomed. Eng.* **46**, 280–290 (1999).

33. Kandel, E. R. in *Principles of Neural Science* (eds Kandel, E. R., Schwartz, J. H. & Jessell, T. M.) 19–35 (McGraw-Hill, 2000).

34. Kozai, T. D. Y. *et al.* Ultrasmall implantable composite microelectrodes with bioactive surfaces for chronic neural interfaces. *Nat. Mater.* **11**, 1065–1073 (2012).

35. Ikedo, A., Kawashima, T., Kawano, T. & Ishida, M. Vertically aligned silicon microwire arrays of various lengths by repeated selective vapor-liquid-solid growth of n-type silicon/n-type silicon. *Appl. Phys. Lett.* **95**, 033502 (2009).

Acknowledgments

Author contributions

A.F., H.K., M.I. and T.K. designed the project. A.F., H.K., T.K. and T.K. performed the project. A.F., H.K., T.K. and T.K. analyzed the data. A.F., H.K. and T.K. prepared the manuscript.

Additional information

Supplementary information accompanies this paper at http://www.nature.com/scientificreports

Competing financial interests: The authors declare no competing financial interests.

How to cite this article: Fujishiro, A., Kaneko, H., Kawashima, T., Ishida, M. & Kawano, T. *In vivo* neuronal action potential recordings via three-dimensional microscale needle-electrode arrays. *Sci. Rep.* **4**, 4868; DOI:10.1038/srep04868 (2014).